



# Origin of localized fast mantle flow velocity in numerical models of subduction

Magali I. Billen

Department of Geology, University of California, One Shields Avenue, Davis, California 95616, USA  
(mibillen@ucdavis.edu)

Margarete Jadamec

Department of Geology, Brown University, 324 Brook Street, Box 1846, Providence, Rhode Island 02906, USA

[1] The origin of localized fast mantle flow near subduction zones found in regional (Jadamec and Billen, 2010, 2012) and global (Stadler et al., 2010; Alisic et al., 2010) numerical models using non-Newtonian rheology is explored using 3D models with simple geometry. Two suites of models, using both a free slab and a slab attached to a lithospheric layer, are presented to determine (1) the origin of high magnitudes of mantle flow (>50 cm/yr) and (2) focusing of flow within the mantle wedge, with mantle wedge velocities up to two times higher than slab sinking velocities. The rheology in the models is either Newtonian with a prescribed low viscosity wedge (LVW) or non-Newtonian wherein low viscosity regions form in response to high stress surrounding the sinking slab. The results show that there are two aspects of the models that lead to localized fast velocities: reduction in the mantle viscosity surrounding the sinking slab leads to faster overall flow rates induced by the negative buoyancy of the sinking slab; and geometric effects that are caused by lateral variations in viscosity, including retrograde pivoting motion of the slab.

**Components:** 9900 words, 9 figures, 3 tables.

**Keywords:** numerical models; rheology; subduction.

**Index Terms:** 8120 Tectonophysics: Dynamics of lithosphere and mantle: general (1213); 8155 Tectonophysics: Plate motions: general (3040).

**Received** 1 September 2011; **Revised** 19 December 2011; **Accepted** 19 December 2011; **Published** 27 January 2012.

Billen, M. I., and M. Jadamec (2012), Origin of localized fast mantle flow velocity in numerical models of subduction, *Geochem. Geophys. Geosyst.*, 13, Q01016, doi:10.1029/2011GC003856.

## 1. Introduction

[2] The motion of tectonic plates at the surface of the earth is driven by thermochemical convection in the mantle, in which the plates form as the top thermal boundary layer and contribute to the convective system by advecting cold material deep into the mantle in subduction zones [Schubert et al.,

2001]. With this convective view of subducting plates comes the expectation that tectonic plates move at roughly the same speed as the mantle. However, rate of flow for any portion of the mantle depends on the local viscosity structure and distribution of buoyancy forces. The rigidity of the plates and subducting slabs is a result of the strong temperature-dependent viscosity of mantle minerals and cooling at the surface, while the lower viscosity

of the asthenosphere results not only from its warmer temperature, but also from the stress-dependence (i.e., non-Newtonian viscosity) of mantle minerals, higher water content and perhaps melt [Karato and Wu, 1993; Hirth and Kohlstedt, 2003]. In global-scale models the low viscosity of the asthenosphere can lead to convective modes in which the flow velocity of the asthenosphere is higher than the plate velocity [Höink and Lenardic, 2010; Becker and Kawakatsu, 2011; M. Gérault et al., The role of slabs and oceanic plate geometry for the net rotation of the lithosphere, trench motions and slab return flow, submitted to *Geochemistry, Geophysics, Geosystems*, 2011].

[3] In addition to the global low viscosity asthenosphere, in numerical models of subduction zones the large driving stress of a sinking slab and the non-Newtonian response of the mantle leads to the formation of localized low viscosity zones in the mantle wedge and surrounding the tip of short slabs [Jadamec and Billen, 2010; Stadler et al., 2010; Alisic et al., 2010; Jadamec and Billen, 2012]. The viscosity within these localized regions can be as low as  $10^{18}$  Pa·s: 2–3 orders of magnitude lower than the asthenosphere. In these numerical models the localized low viscosity regions are correlated with fast mantle flow velocities of 50–90 cm/yr [Jadamec and Billen, 2010; Stadler et al., 2010; Alisic et al., 2010; Jadamec and Billen, 2012]. While these are not the first models to exhibit faster flow velocities close to the slab [Kincaid and Griffiths, 2003; Schellart, 2004; Funiciello et al., 2006; Stegman et al., 2006], they are the first models to predict localized mantle flow velocities that are more than two times faster than the sinking rate of the slab and 10–20 times faster than surface plate motions [Jadamec and Billen, 2010; Stadler et al., 2010; Alisic et al., 2010; Jadamec and Billen, 2012].

[4] Both laboratory [Kincaid and Griffiths, 2003; Schellart, 2004; Funiciello et al., 2006] and numerical [Stegman et al., 2006; Conder and Wiens, 2007; Di Giuseppe et al., 2008] models using Newtonian viscosity (with or without yielding) have shown that retreating motion of the slab with steepening induces a strong toroidal component of flow around the slab that couples to the poloidal flow induced by down-dip sinking of the slab to increase mantle flow velocities above the slab (in the mantle wedge) and below and behind the tip of shorter slabs. For example [Kincaid and Griffiths, 2003] found mantle wedge flow velocities of 1.1–1.6 times the down-dip component of slab motion and Funiciello et al. [2006] found mantle flow rates

of 150% of the trench velocity, but in almost all these models mantle flow rates are less than 5–15 cm/yr, comparable to observed surface plate motions. The exception is the study by *Conder and Wiens* [2007] which imposed slab-parallel flow on the order of 46 cm/yr in order to match shear wave splitting measurements in the Tonga back-arc. Large mantle-to-lithosphere flow ratios were also generated in 2D and 3D instantaneous models with an imposed low viscosity wedge (LVW) [Billen and Gurnis, 2001; Billen et al., 2003] with strong localization of flow within the weak region, but this result was not highlighted in those studies. Therefore, the very fast and localized mantle flow velocities predicted by the recent studies using non-Newtonian rheology [Jadamec and Billen, 2010; Stadler et al., 2010; Alisic et al., 2010; Jadamec and Billen, 2012] are unprecedented in previous published studies.

[5] Fast localized mantle flow velocities surrounding the slab also generate large shear strains and therefore are one mechanism by which to create strong seismic anisotropy [Kaminiski and Ribe, 2002; Karato et al., 2008]. Observations of seismic anisotropy in subduction zones are characterized by rapid changes in orientation above the mantle wedge [Russo and Silver, 1994; Smith et al., 2001; Fischer et al., 2000; Long and Silver, 2008; Christensen and Abers, 2010] indicating either rapid changes in the orientation of shear, or changes in the active slip system of olivine under rapidly varying temperature-stress conditions, or both [Karato et al., 2008]. Kinematically-driven wedge flow models using non-Newtonian rheology show that changes in along-strike dip of slabs can generate slab-parallel stretching in the mantle wedge consistent with observation of seismic anisotropy [Kneller and van Keken, 2007, 2008]. Toroidal flow around the edge of a slab generated by slab roll-back can also generate slab-parallel alignment of fabric [Buttles and Olson, 1998]. In particular, observations of seismic anisotropy in central Alaska were used to constrain the slab structure and rheology in models with fast localized mantle wedge flow velocities [Jadamec and Billen, 2010, 2012].

[6] Because the recent studies [Jadamec and Billen, 2010; Stadler et al., 2010; Alisic et al., 2010; Jadamec and Billen, 2012] predict mantle flow velocities surrounding slabs faster than any previous studies, these surprising results have generated discussion about the physical origin of these regions of fast mantle flow, including questions about model convergence, applicability of

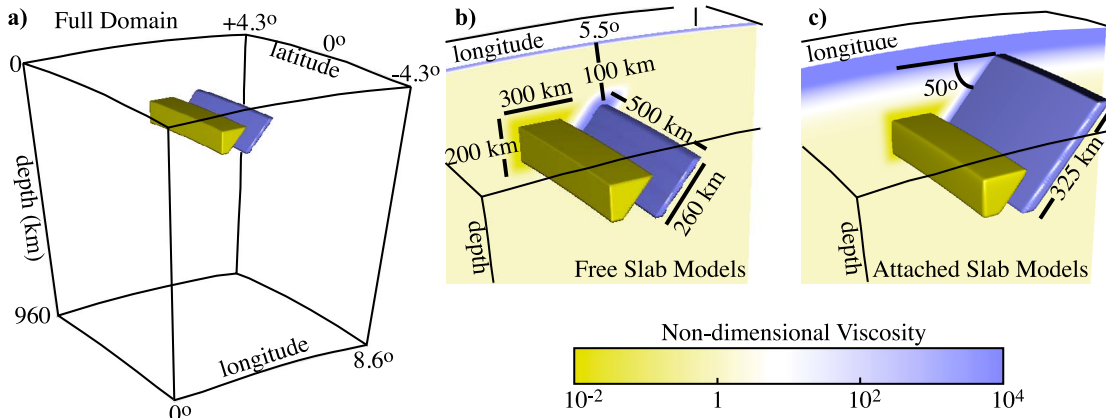


**Figure 1.** Model domain, slab and low viscosity wedge geometry. (a) Full model domain (free slab shown). (b) Free slab model geometry (slab dip shown in Figure 1c). (c) Attached slab model geometry. All dimensions are the same as in Figure 1b except as indicated. Blue isosurface: slab geometry at 700°C. Yellow isosurface: weak mantle wedge geometry at a viscosity of  $10^{-2}\eta_{ref}$ .

instantaneous solutions, and implementation of the non-Newtonian rheology. Because these recent models also used complex 3D geometries for subduction zone buoyancy and viscosity, based on constraints from seismology (e.g., seismicity, tomography), this made it more difficult to clearly demonstrate the physical cause of both the high magnitudes of flow and the localized fast flow velocities, or to benchmark the numerical solutions against analytic solutions. The purpose of this study is to present 3D numerical models with a simple slab and mantle wedge geometry, using either Newtonian or non-Newtonian rheology, and simple variation in parameters in order to verify that subduction driven fast localized flow velocities are not a numerical artifact.

## 2. Methods

[7] We use the mantle deformation and convection code **CitcomS**, which employs the finite element method to solve the standard equations of motions governing viscous flow of an incompressible fluid subject to the Boussinesq approximation [Zhong *et al.*, 2000; Tan *et al.*, 2006]. We are only interested in the instantaneous flow resulting from solution of the conservation of momentum equation subject to the incompressibility constraint imposed by the conservation of mass (although we do run a subset of models forward in time to verify the results are unchanged). We note that the previous models of the Alaska subduction zone [Jadamec and Billen, 2010, 2012] used an earlier version of this code referred to as CitcomCU [Zhong, 2006; Moresi and Gurnis, 1996] and the global models with fast mantle flow of [Stadler *et al.*, 2010; Alisic

*et al.*, 2010] used the finite element code Rhea. The finite element solutions are implemented identically in the two versions of the Citcom code. For the non-Newtonian models we use the same composite rheology that we implemented in CitcomCU in this version (3.1.1) of **CitcomS** (described below). In the following section, we present a detailed description of the model design such that these models could be used to benchmark future codes.

### 2.1. Model Setup

[8] The model domain (Figure 1) is centered at the equator and extends from 85.68° to 94.32° in co-latitude ( $\theta$ ), 0° to 8.64° in longitude ( $\phi$ ) and 5411 to 6371 km in radius (e.g., approximately 960 km in each direction). The element spacing is constant in all directions: 0.045° (5.0 km) in co-latitude and longitude and 5.0 km in radius (193 nodes in each direction). All boundaries are free-slip. The top and bottom boundaries have fixed temperatures of 0°C and 1400°C, respectively, while the sidewalls are insulating.

[9] Two model configurations are presented: the first has a free slab with no lithospheric layer (Figure 1b) and the second has a slab attached to a lithospheric layer (Figure 1c). In both models the slab is defined as a rectangular parallelepiped with a trench-perpendicular (longitude) thickness of 65 km and trench-parallel (co-latitude) length of 555 km (i.e., 5°). For the free slab, the top of the slab is at 100 km depth (centered at a longitude of 5.5°), while for the attached slab, the top of the slab is at 10 km (centered at a longitude of 6.18°). Both slabs have a 50° dip and extend to 300 km depth.

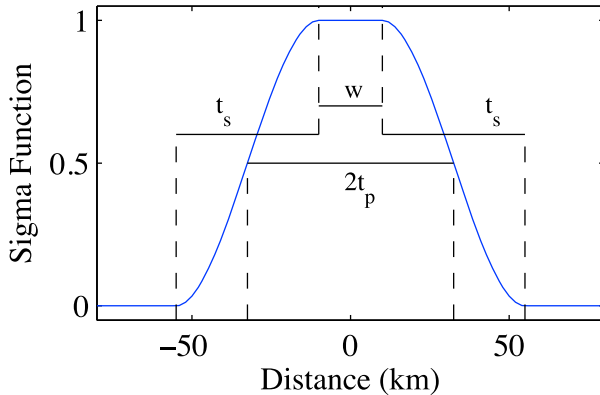


**Figure 2.** Sigma function used to define temperature and viscosity structures with edges smoothed over a specific number of elements. Width  $t_s$  is the distance over which  $S(d)$  decreases from one to zero and  $w$  is the width of the center region kept at a constant value of one. We define the slab width and LVW widths to be  $2t_p$ , corresponding to the point where  $S(d_n)$  has a value of 0.5.

The minimum temperature within the slab is 700°C. For the attached slab, the lithospheric temperature is defined using the half-space cooling model with an age of 60 My:

$$T_{half} = (T_m - T_o) \operatorname{erf}\left(\frac{z}{2\sqrt{\kappa t}}\right) \quad (1)$$

where  $T_m = 1400^\circ\text{C}$ ,  $T_o = 0^\circ\text{C}$ ,  $\kappa = 10^{-6} \text{ m}^2/\text{s}$ ,  $z$  is depth, and  $t$  is plate age [Turcotte and Schubert, 1982]. Note, the attached slab models represent an end-member case in which we have intentionally omitted a low viscosity shear zone between the overriding and subducting plates and therefore the subducting plate is not free to be pulled into the mantle by the slab. Jadamec and Billen [2012] show that it is the shear zone viscosity and yield stress which control the degree of coupling between the sinking slab and subducting plate at the surface.

[10] In models with an imposed low viscosity wedge (LVW), the weak region extends from 120 to 280 km depth (Figure 1b). The boundary of the weak zone adjacent to the slab has a 50° dip (parallel to the slab), whereas the opposite boundary is vertical. The width of the top of the weak zone in longitude is 335 km, whereas the bottom is 45 km. The weak zone extends over the same trench-parallel length as the slab (5° or 555 km) centered at the equator. The size and geometry of the LVW was chosen to match the weak region that emerges in models using non-Newtonian rheology. We do not vary the size or geometry of the LVW, but shape of LVW has been study previously [Billen et al., 2003].

## 2.2. Smoothed Structures

[11] To create smoothed edges for the slab temperature anomaly and LVW we use the following smoothing function,  $S$  (referred to as the sigma-function [Jadamec, 2008]), which varies from values of one to zero as a function of distance from the center of the slab or LVW outwards (Figure 2):

$$S(d_n) = 1 - d_n^2(3 - 2d_n); d_n \geq t_p - 0.5t_s \quad (2)$$

$$S(d_n) = 1; d_n < t_p - 0.5t_s \quad (3)$$

where  $d_n$  is a non-dimensional distance given by,

$$d_n = \frac{(d - t_p + 0.5t_s)}{t_s} \quad (4)$$

where  $d$  is distance from the center of the slab or LVW,  $t_p = 0.5(w + t_s)$ ,  $t_s$  is the distance over which  $S(d_n)$  decreases from one to zero and  $w$  is the width of the center region ( $S = 1$ ).

[12] Using the  $S$  function we prescribe temperature and viscosity variations that give rise to viscosity gradients of less than a factor of three change across one element for models with the largest viscosity variations. Limiting the viscosity gradient across an element in this way has been shown to insure accurate solutions of the momentum equation in the presence of large viscosity contrasts [Moresi et al., 1996]. For the slab temperature anomaly, the constant temperature region is fixed by  $w$  values of 20 km (longitude), 465 km (co-latitude) and 110 km (radius). The smooth region width ( $t_s$ ) is defined to be 9 elements or 45 km on all sides. For the LVW, the constant viscosity region is fixed by  $w$  values of 300 km for the top and 10 km for the bottom (longitude), 485 km (co-latitude) and 110 km (radius). The smooth region is 7 elements or 35 km on all sides.

[13] The final slab temperature or LVW structure is defined by multiplying the three sigma functions, one for each of the three spherical coordinate directions. For the slab temperature:

$$T(\phi, \theta, r) = T_m - \Delta T [S_{s,\phi}(d_\phi) S_{s,\theta}(d_\theta) S_{s,r}(d_r)] \quad (5)$$

where  $\Delta T = 700^\circ\text{C}$  and the subscript,  $s$ , indicates slab-related sigma functions. For the attached-slab models,  $T_m$  is replaced with  $T_{half}$  (equation (1)). Similarly, for the LVW the weakening factor,  $A_{wk}$ , is defined by:

$$A_{wk}(\phi, \theta, r) = S_{w,\phi}(d_\phi) S_{w,\theta}(d_\theta) S_{w,r}(d_r) \quad (6)$$

**Table 1.** Viscous Flow Law Parameters for Olivine Used in Equation (12)<sup>a</sup>

Creep Parameter	df	ds
$F_{\text{exp}}^{\text{b}}$	0.333	0.308
$n$	1	3.5
$A^{\text{c}}$	0.28	$2.5 \times 10^{-21}$
$d_{\text{um}} (\text{mm})$	10	—
$d_m (\text{mm})$	84	—
$p$	3	0
$C_{\text{OH}} (\text{ppm/Si})$	1000	1000
$r$	1.0	1.2
$E (\text{kJ/mol})$	335	480
$V_{\text{um}} (\times 10^{-6} \text{ m}^3/\text{mol})$	4.0	11.0
$V_{\text{lm}} (\times 10^{-6} \text{ m}^3/\text{mol})$	1.5	—

<sup>a</sup>Hirth and Kohlstedt [2003].

<sup>b</sup> $F_{\text{exp}}$  is the experimental geometry modification parameter [Gerya, 2010].

<sup>c</sup> $A$  has been reduced by a factor 3.5 from the values of 1 (df) and  $90 \times 10^{-21}$  (ds) given by Hirth and Kohlstedt [2003] following a correction for the water calibration in those experiments [Bell et al., 2003].

where the subscript,  $w$ , indicates LVW related sigma functions.

### 2.3. Rheology

[14] We run one set of models with Newtonian rheology with and without an imposed LVW and a second set of models using non-Newtonian rheology.

[15] For the Newtonian rheology models, there are two parts to the non-dimensional viscosity structure: the temperature-dependence for the slab and an imposed low viscosity region for the wedge. The non-dimensional temperature-dependent viscosity is given by:

$$\eta'(T) = \exp[E(1.0 - T')] \quad (7)$$

where  $T' = T/T_m$  is the non-dimensional temperature and  $E = 18.425$  is the non-dimensional activation energy chosen to give a maximum non-dimensional viscosity of  $10^4$  for a non-dimensional temperature of 0.5, which is similar to the viscosity gradient found from the composite viscosity law used in the non-Newtonian models here and previously [Jadamec and Billen, 2010]. In addition, a maximum viscosity cut-off value of  $10^2$  or  $10^4$  is used to vary the maximum strength of the slab.

[16] The non-dimensional viscosity for the imposed LVW in the wedge is given by:

$$\eta'_{\text{wk}} = 10^{[A_{\text{wk}} \log_{10}(\eta'_{\min})]} \quad (8)$$

where  $\eta'_{\min}$  is the minimum non-dimensional viscosity applied to the LVW. The final value of the non-dimensional viscosity is found by combining  $\eta'(T)$  and  $\eta'_{\text{wk}}$ :

$$\eta' = 10^{[\log_{10}(\eta'(T)) + \log_{10}(\eta'_{\text{wk}})]} \quad (9)$$

These values are then scaled by the reference viscosity  $\eta_{\text{ref}}$  defined in conjunction with the Rayleigh number ( $Ra = (\rho_{\text{ref}}\alpha(T_m - T_o)gR_e^3)/(\kappa\eta_{\text{ref}})$ , where  $\rho_{\text{ref}} = 3300 \text{ kg/m}^3$  is the reference density,  $\alpha = 2 \times 10^{-5} \text{ }^{\circ}\text{C}^{-1}$  is the thermal expansion coefficient, and  $R_e = 6371 \text{ km}$  is earth's radius).

[17] For the small group of non-Newtonian rheology models presented, we use the same composite viscosity equation and flow law parameters as used by Jadamec and Billen [2010]. For these models, we only vary the yield strength or the minimum viscosity cut-off value. The composite viscosity is defined as:

$$\eta_{\text{comp}} = \min(\eta_{\text{eff}}, \sigma_y/\dot{\epsilon}_{II}) \quad (10)$$

where  $\eta_{\text{eff}}$  is the effective viscosity,  $\sigma_y$  is the yield stress (1000 MPa, 500 MPa or 300 MPa) and  $\dot{\epsilon}_{II}$  is the second invariant of the strain rate tensor. The effective viscosity, for deformation at constant stress, is,

$$\eta_{\text{eff}} = \frac{\eta_{\text{df}}\eta_{\text{ds}}}{\eta_{\text{df}} + \eta_{\text{ds}}} \quad (11)$$

where  $\eta_{\text{df}}$  and  $\eta_{\text{ds}}$  are the diffusion and dislocation viscosity for olivine, respectively, determined from experimentally-derived flow laws [Hirth and Kohlstedt, 2003]. The viscosity flow law for olivine, for constant water content and no melt, is,

$$\eta_{\text{df},\text{ds}} = F_{\text{exp}} \left( \frac{d^p}{AC_{\text{OH}}^r} \right)^{1/n} \dot{\epsilon}_{II}^{\frac{1-n}{n}} \exp \left[ \frac{E + P_{lc}V}{nRT_t} \right] \quad (12)$$

where  $F_{\text{exp}}$  is the experimental geometry modification parameter;  $d$  is the grain size;  $p$  is the grain size exponent;  $A$  is the pre-exponential factor;  $C_{\text{OH}}$  is the hydroxyl concentration;  $r$  is the water concentration exponent;  $n$  is the stress exponent;  $E$  is the activation energy; and  $V$  is the activation volume (Table 1). The temperature,  $T_t$ , is the temperature in the model plus an adiabatic temperature gradient of  $0.3^{\circ}\text{C}/\text{km}$ . The viscosity depends on the

lithostatic pressure (fit linearly from the surface to 670 km),

$$P_{lc} = (-1/\beta) \log(1 - \rho_0 g \beta z) \quad (13)$$

where  $z$  is depth in meters, and  $\beta = 4.3 \times 10^{-12}$  Pa $^{-1}$  is the compressibility [Turcotte and Schubert, 1982].

[18] Grain size is chosen to match the upper mantle viscosity inferred from post-glacial rebound [Forte and Mitrovica, 1996], and to control the viscosity of the Newtonian rheology lower mantle. An experimental geometry modification factor,  $F_{exp}$ , modifies the composite viscosity of Hirth and Kohlstedt [2003] to account for the conversion of the flow law from experimental deformation geometry (axial-compression strain rate and differential stress) to the numerical model, which uses the second invariants of strain rate and stress [Gerya, 2010]. Note also that the pre-exponential factor has been modified from work by Hirth and Kohlstedt [2003] to account for a water content calibration error [Bell et al., 2003]. These two changes to the flow law (adding  $F$  and modifying  $A$ ) almost cancel each other leaving the flow-law magnitudes essentially unchanged from previous studies [e.g., Billen and Hirth, 2005, 2007; Andrews and Billen, 2009; Burkett and Billen, 2009; Jadamec and Billen, 2010].

[19] The composite viscosity is solved for iteratively with the model flow (and nondimensionalized by the reference viscosity). In the first iteration the strain rate is set to  $1 \times 10^{-15}$  Pa-s, corresponding to the transition strain rate ( $\eta_{df} = \eta_{ds}$ ) at 250 km. Subsequent iterations use the strain rate from the previous velocity solution: iterations continue until the global change in the velocity field from one iteration to the next is less than 1%.

## 2.4. Quantifying Flow Focusing

[20] We refer to flow in which the magnitude of the return flow induced by sinking of the slab is higher (than found in a uniform background viscosity model) in some localized region of the mantle as flow localization or flow focusing. We quantify this behavior by measuring the ratio of the maximum wedge flow velocity magnitude,  $v_{wedge}$ , to the maximum slab velocity magnitude,  $v_{slab}$  (defined as the region at a constant non-dimensional temperature of 0.5),

$$F = \frac{v_{wedge}}{v_{slab}} \quad (14)$$

The value of  $F$  that indicates flow focusing is occurring depends on the model geometry (i.e., free versus attached slabs, and uniform background viscosity or LVW).

## 3. Results

[21] We present two sets of models to address the origin of localized high velocity flow in the mantle surrounding subducting slabs. The first set of models uses Newtonian or non-Newtonian (composite) viscosity without an imposed LVW (section 3.1, Table 2) to investigate the origin of large magnitude mantle flow velocities. Both free slab (Figure 1b) and attached slab (Figure 1c) model geometries are used. The results of these models are compared to the analytic solution for the sinking rate of a Stokes ellipsoid [Kerr and Lister, 1991]. We also present a subset of models to test the effect of yield stress (attached-slabs only; AY, Table 2).

[22] The second set of models uses Newtonian viscosity with an imposed LVW (section 3.2, Table 3) to investigate the cause of flow velocities in the mantle wedge that exceed the slab sinking velocity (i.e., flow focusing). Both free slab (Figure 1b) and attached slab (Figure 1c) model geometries are used. For each model geometry we vary the maximum slab viscosity ( $\eta'_{slab} = 10^0\text{--}10^4$ ) and the minimum weak region viscosity ( $\eta'_{main} = 10^{-1}\text{--}10^{-3}$ ) using a fixed background reference viscosity,  $\eta_{ref} = 10^{20}$  Pa-s. We also present a subset of models with a reduced background viscosity (FwR, AwR; Table 3).

### 3.1. Sinking Velocity of Free and Attached Slabs

[23] The magnitude of flow velocities induced by sinking of a free or attached slab depends on the sinking rate of the slab. To first order the rate of sinking can be approximated analytically by the Stokes sinking velocity for an appropriately-shaped ellipsoid [Kerr and Lister, 1991]:

$$V_e = S_e V_s \quad (15)$$

where  $V_e$  is the ellipsoid sinking velocity,  $S_e$  is a shape factor that takes into account the relative lengths of the ellipsoidal axis and orientation of the ellipsoid in the fluid [Kerr and Lister, 1991, equation 4], and  $V_s$  is the sinking velocity of a sphere:

$$V_s = \frac{g(\rho_s - \rho_m)D^2}{18\eta_m} \quad (16)$$

**Table 2.** Model Parameters and Flow Field Results for Models With No LVW<sup>a</sup>

Model	$\eta'_{\min}$	$\eta'_{\text{slab}}$	$\eta_{\text{ref}} (\text{Pa-s})$	$v_{\text{wedge}} (\text{cm/yr})$	$v_{\text{slab}} (\text{cm/yr})$	$F$
<i>Free-Slab Models</i>						
F0	$10^0$	$10^0$	$10^{20}$	10.58	18.68	0.57
F1	$10^0$	$10^2$	$10^{20}$	5.73	8.79	0.65
F2	$10^0$	$10^4$	$10^{20}$	4.30	7.67	0.56
F2R10	$10^0$	$10^4$	$10^{19}$	42.97	76.65	0.56
F2R100	$10^0$	$10^4$	$10^{18}$	429.76	766.52	0.56
F2nn1	$10^0$	$10^4$	$10^{20}$	5.76	10.59	0.54
F2nn2	$10^{-1}$	$10^4$	$10^{20}$	51.38	97.06	0.53
	(time step 5)			51.58	99.56	0.52
	(time step 10)			51.82	101.66	0.51
<i>Attached-Slab Models</i>						
A0	$10^0$	$10^0$	$10^{20}$	10.87	19.77	0.55
A1	$10^0$	$10^2$	$10^{20}$	2.75	2.75	1.00
A2	$10^0$	$10^4$	$10^{20}$	1.58	1.14	1.38
A2R10	$10^0$	$10^4$	$10^{19}$	15.83	11.44	1.38
A2R100	$10^0$	$10^4$	$10^{18}$	158.34	114.41	1.38
A2nn1	$10^0$	$10^4$	$10^{20}$	5.41	5.70	0.95
A2nn2	$10^{-1}$	$10^4$	$10^{20}$	42.09	46.24	0.91
	(time step 5)			41.93	45.80	0.92
	(time step 10)			41.21	44.93	0.92
A2Y3	$10^0$	$10^4$	$10^{20}$	9.73	16.30	0.60
A2Y5	$10^0$	$10^4$	$10^{20}$	8.10	12.93	0.63
A2Y10	$10^0$	$10^4$	$10^{20}$	3.92	6.89	0.57
A2nnY3	$10^{-1}$	$10^4$	$10^{20}$	104.25	173.02	0.60
A2nnY5	$10^{-1}$	$10^4$	$10^{20}$	99.84	161.11	0.62
A2nnY10	$10^{-1}$	$10^4$	$10^{20}$	82.12	134.91	0.61

<sup>a</sup>These models are used to understand the origin of high velocity magnitudes induced by sinking of free or attached slabs. Model names: F is free slab, A is attached slab, R10 is reference viscosity reduced by  $\times 10$ , R100 is reference viscosity reduce by  $\times 100$ , nn is non-Newtonian, Y3 is  $\sigma_y = 300 \text{ MPa}$ , Y5 is  $\sigma_y = 500 \text{ MPa}$ , Y10 is  $\sigma_y = 1000 \text{ MPa}$ .

where  $g$  is gravitational acceleration,  $\rho_s$  and  $\rho_m$  are the densities of the rigid sphere and fluid mantle, respectively,  $D$  is the diameter of the sphere, and  $\eta_m$  is the viscosity of the mantle. Because the ellipsoid sinking velocity is simply proportional to the sinking velocity of a sphere, the sinking rate of a slab with a defined density contrast scales inversely with the viscosity of the surrounding fluid (equation (16)). Therefore, one would expect a reduction in mantle viscosity by a factor 10 to result in an increase in the sinking rate of the slab by a factor of 10. It follows from this analysis that mantle velocities of 50 to 100 cm/yr, as found in subduction models using non-Newtonian rheology discussed in the introduction, are not unexpected if the slab (or a portion of the slab) can sink freely: the non-Newtonian rheology results in a local reduction in viscosity surrounding the slab by up to a factor of 100 with respect to the background mantle viscosity.

[24] The numerical experiments using a free slab geometry with Newtonian rheology and varying the background reference viscosity reproduce the inverse scaling between slab sinking velocity and mantle viscosity (F2, F2R10, F2R100; Table 2 and Figure 3a) predicted by the analytic solution for

a sinking ellipsoid (ellipsoid dipping 50° with axis of 50, 100 and 500 km,  $D = 186 \text{ km}$ , and  $\rho_s - \rho_m = 23 \text{ kg/m}^3$ ). Sinking rates increase from about 4 cm/yr to 40 cm/yr for a reduction in the reference viscosity from  $10^{20} \text{ Pa-s}$  to  $10^{19} \text{ Pa-s}$ : a viscosity drop typical of models using non-Newtonian rheology. These models use a maximum viscosity of the slab of  $10^4$  times the reference viscosity: lower viscosity slabs (F0, F1) sink at higher velocities due to lower viscous shear stress between the slab and surrounding material. Free slab models with a non-Newtonian viscosity also exhibit the same scaling between slab sinking rate and the minimum viscosity (F2nn1, F2nn2, Table 2 and Figure 3a). In both Newtonian and non-Newtonian models (Figure 4a) sinking of a free slab is characterized by nearly radial sinking of the slab with a broad return flow on either side of the slab and flow converging above the slab. The fastest velocities are concentrated within and below the slab and decrease rapidly with distance from the slab (Figure 4a).

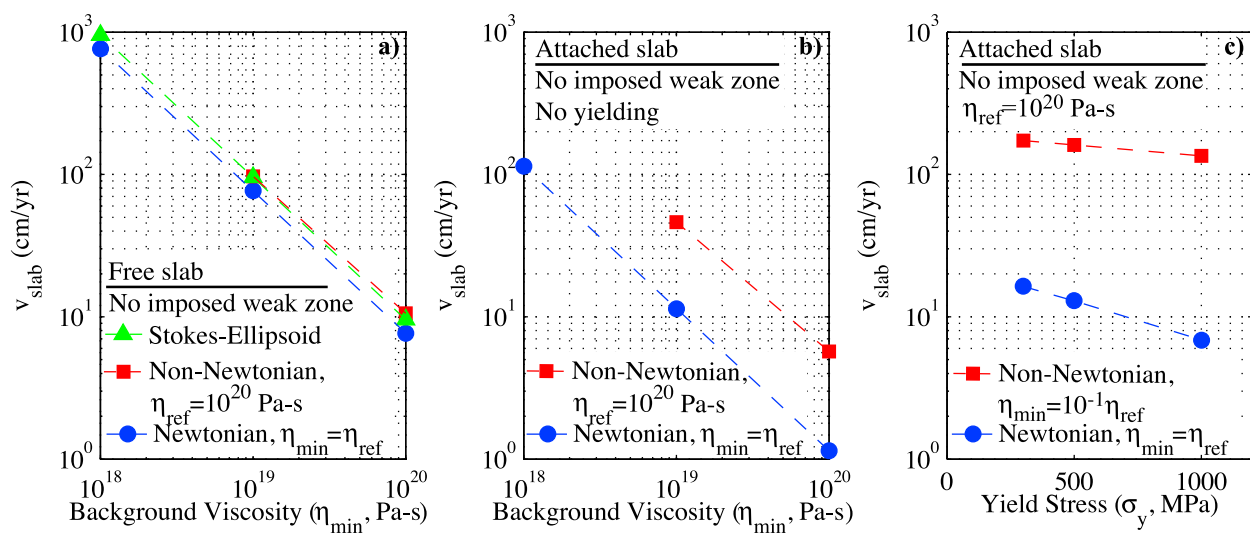
[25] Attached slab models exhibit a similar scaling of slab velocity with background viscosity for both Newtonian (A2, A2R10, A2R100; Table 2 and

**Table 3.** Model Parameters and Flow Field Results for Models With a Low Viscosity Wedge<sup>a</sup>

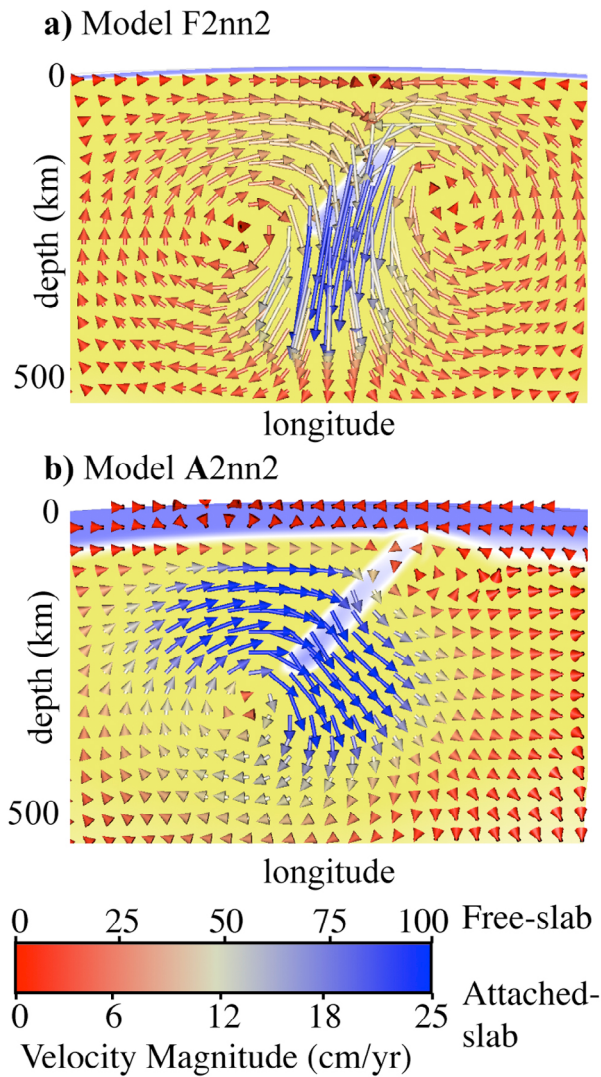
Model	$\eta'_{wk}$ <sup>b</sup>	$\eta'_{slab}$	$\eta_{ref}$ (Pa-s)	$v_{wedge}$ (cm/yr)	$v_{slab}$ (cm/yr)	$F$
<i>Free-Slab Models</i>						
Fw1	$10^{-1}$	$10^2$	$10^{20}$	6.22	10.39	0.60
Fw2	$10^{-1}$	$10^4$	$10^{20}$	5.09	9.20	0.55
	(time step 5)			5.06	9.14	0.55
	(time step 10)			5.04	9.21	0.55
Fw3	$10^{-2}$	$10^2$	$10^{20}$	8.31	11.13	0.75
Fw4	$10^{-2}$	$10^4$	$10^{20}$	7.39	9.82	0.75
Fw5	$10^{-3}$	$10^2$	$10^{20}$	10.62	11.45	0.93
Fw6	$10^{-3}$	$10^4$	$10^{20}$	9.26	10.08	0.92
Fw2R10	$10^{-1}$	$10^4$	$10^{19}$	50.91	91.98	0.55
Fw2R100	$10^{-1}$	$10^4$	$10^{18}$	509.13	919.80	0.55
Fw4R10	$10^{-2}$	$10^4$	$10^{19}$	73.90	98.22	0.75
Fw4R100	$10^{-2}$	$10^4$	$10^{18}$	738.98	982.24	0.75
<i>Attached-Slab Models</i>						
Aw1	$10^{-1}$	$10^2$	$10^{20}$	4.07	3.72	1.09
Aw2	$10^{-1}$	$10^4$	$10^{20}$	2.09	1.32	1.59
	(time step 5)			2.14	1.33	1.60
	(time step 10)			2.14	1.37	1.56
Aw3	$10^{-2}$	$10^2$	$10^{20}$	5.63	4.30	1.31
Aw4	$10^{-2}$	$10^4$	$10^{20}$	2.67	1.40	1.90
Aw5	$10^{-3}$	$10^2$	$10^{20}$	7.03	4.54	1.55
Aw6	$10^{-3}$	$10^4$	$10^{20}$	3.13	1.44	2.18
Aw2R10	$10^{-1}$	$10^4$	$10^{19}$	20.92	13.17	1.59
Aw2R100	$10^{-1}$	$10^4$	$10^{18}$	209.17	131.65	1.59
Aw4R10	$10^{-2}$	$10^4$	$10^{19}$	26.68	14.02	1.90
Aw4R100	$10^{-2}$	$10^4$	$10^{18}$	266.81	140.18	1.90

<sup>a</sup>LWV indicated by ‘w’ in the model name. These models are used to understand the cause of wedge velocity magnitudes that exceed slab velocity magnitudes. Variables and model names are the same as defined in Table 2.

<sup>b</sup> $\eta'_{min}$  is the minimum non-dimensional viscosity in the imposed LWV.



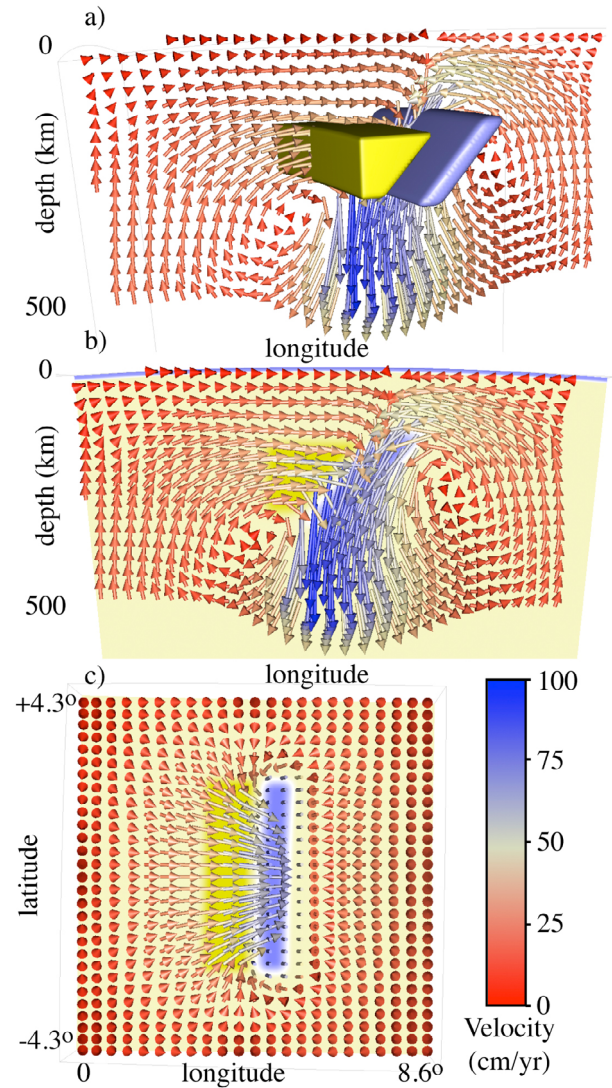
**Figure 3.** Slab sinking velocity results. (a) The magnitude of slab flow velocities for Newtonian models with no imposed weak zone and non-Newtonian models show the same scaling with background viscosity as that predicted for a Stokes ellipsoid. (b) Attached slabs show the same scaling of maximum slab velocity with background viscosity as in the free slab models for both Newtonian and non-Newtonian rheology. (c) Yielding causes the slab to completely detach (see text for discussion): slab flow velocity increases with decreasing yield stress similar to dependence on slab viscosity found in Newtonian free-slab models.



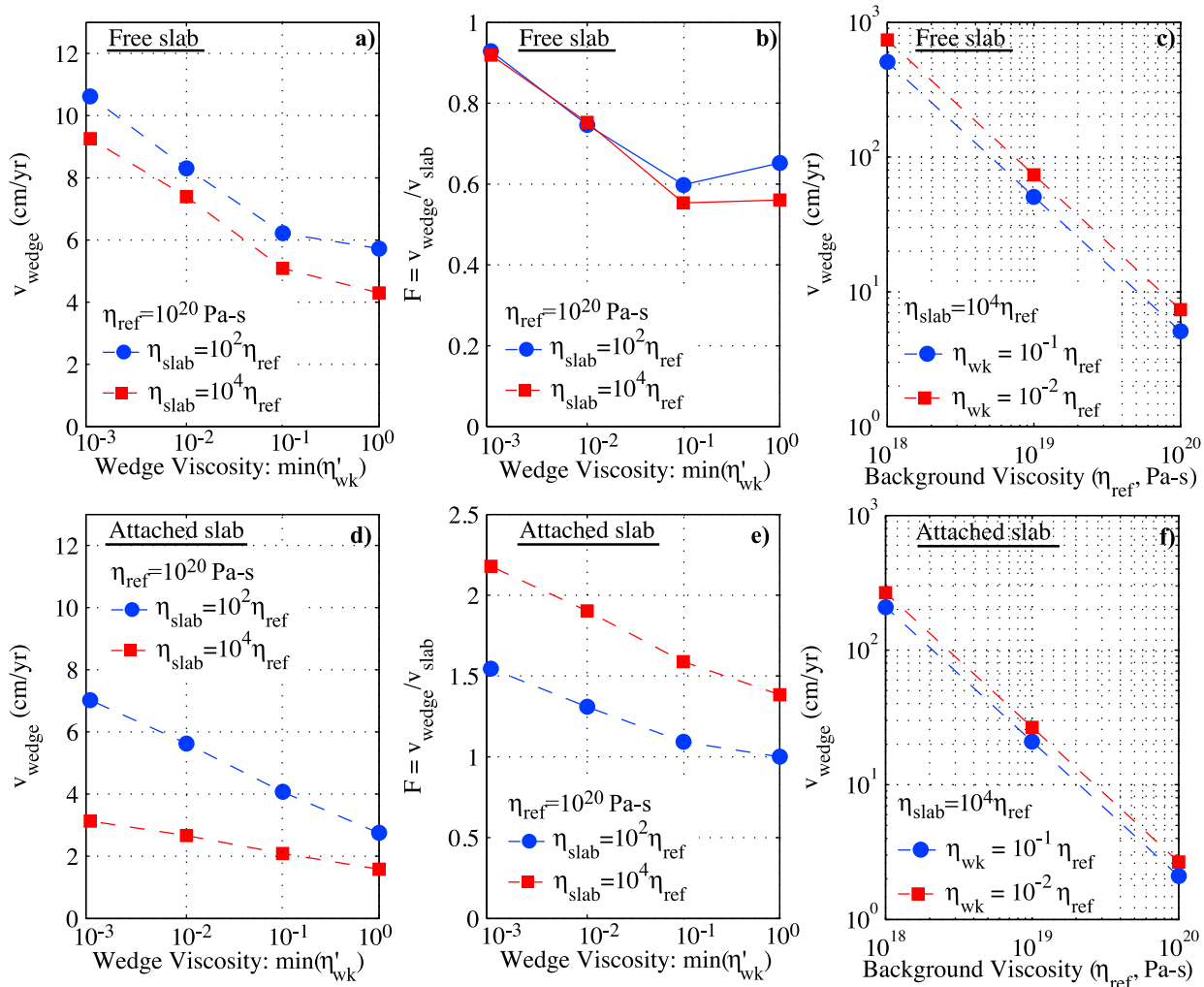
**Figure 4.** Cross section of velocity and viscosity for non-Newtonian models with (a) free slab (Model F2nn2) and (b) attached slab (Model A2nn2). Both models have a minimum viscosity cut-off of  $\eta'_{\min} = 10^{-1}$ . Note predominantly radial sinking for the free slab model, and pivoting motion of attached slab. Color slice is viscosity using the same color scale as in Figure 1. Only a portion of the domain and flow are shown.

Figure 3b) and non-Newtonian rheology (A2nn1, A2nn2), but the sinking rate is significantly higher for non-Newtonian rheology (factor of 5; Figure 3b) and the pattern of flow induced by the slab is quite different from a free slab (Figure 4b). First, the sinking rates for non-Newtonian rheology are higher because the viscosity of the slab in these models decreases and partially decouples the slab from the subducting plate. Second, the pattern of flow is characterized by retrograde pivoting of the slab with flow velocities in and behind the slab

oriented perpendicular to the slab surface, and horizontal flow above the slab in the mantle wedge (Figure 4b). In addition, flow with velocities comparable to (or even higher than) the highest slab velocities extend more than 100 km away from the



**Figure 5.** 3D flow for free slab model Fw4R10. (a) 3D perspective of cross section of flow ( $0^\circ$  latitude) with viscosity isosurfaces for the LVW and slab. Note strong radial component of slab flow. Isosurfaces of LVW and slab in yellow and blue, respectively. Same isosurface and viscosity color scale as in Figure 1. (b) Cross section (same as in Figure 5a) showing merging of flow above the slab and radially directed flow within slab. (c) Map view at  $\sim 150$  km depth showing horizontal flow focused within the LVW. Color slice in Figures 5b and 5c is viscosity for reference, using the same color scale as in Figure 1. Only a portion of the domain and flow are shown.



**Figure 6.** Wedge flow focusing results for Newtonian viscosity models with an imposed LVW showing free-slab models and attached-slab models. (a) Mantle wedge velocity exhibits only a weak dependence on the LVW viscosity. (b) Flow focusing,  $F$ , is higher for lower viscosity in the mantle wedge, but has no dependence on slab viscosity. (c) The magnitude of mantle wedge flow velocities scales directly with the background viscosity (i.e.,  $F$  does not depend on  $\eta_{\text{ref}}$ ). (d) For attached slab models, the maximum wedge velocity increases with decreasing LVW viscosity as in free slab models, but the magnitude is slightly smaller. (e) Focusing of flow in the mantle wedge is stronger in attached slab models ( $F > 2$ ) and is more pronounced for higher viscosity slabs. (f) For attached slab models, the magnitude of mantle wedge flow velocities also scales directly with the background viscosity.

slab in the mantle wedge and below the tip of the slab, but drop off rapidly in the rest of the mantle. (Figure 4b). The attached slab models, therefore, exhibit what we have defined as flow focusing, and we will return to discuss this point in the next section.

[26] This set of models, without an imposed LVW, demonstrates that the high magnitudes of the mantle velocities are not an artifact of the non-Newtonian rheology, but instead high sinking velocities are expected from the reduction in viscosity

that occurs in high stress regions surrounding slabs due to non-Newtonian rheology.

### 3.2. Flow Focusing in the Mantle Wedge

[27] Flow focusing refers to the occurrence of flow velocities, in a region surrounding the slab and induced by slab sinking, that exceed the flow magnitude of the slab itself. In this set of models we investigate the origin of flow focusing in the mantle wedge caused by an imposed reduction in wedge viscosity.

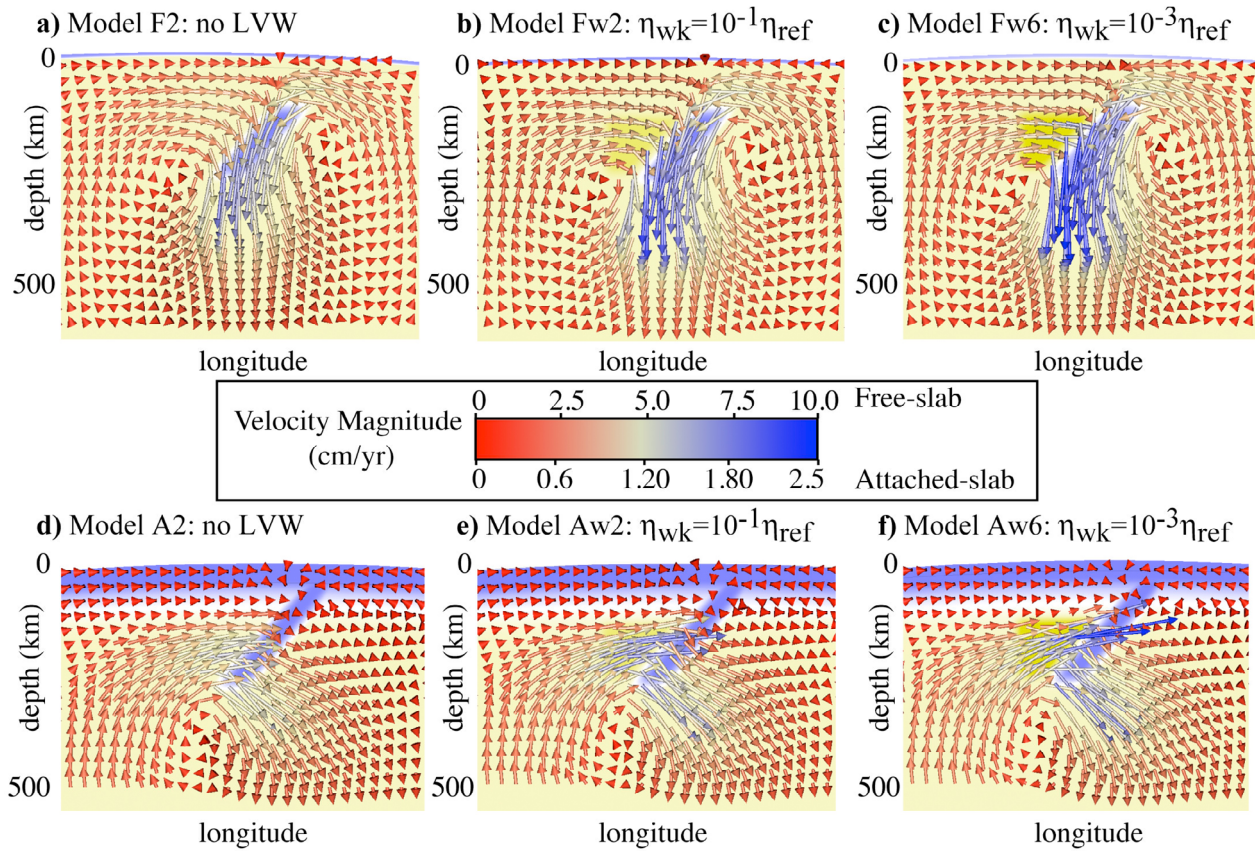


**Figure 7.** Effect of LVW viscosity on flow pattern and magnitudes for models with reference viscosity,  $\eta_{ref} = 10^{20}$  Pa·s. (a–c) Free slab models (F2, Fw2, Fw6) and (d–f) attached slab models (A2, Aw2, Aw6), with no LVW (Figures 7a and 7d),  $\eta'_{wk} = 10^{-1}$  (Figures 7b and 7e), and  $\eta'_{wk} = 10^{-3}$  (Figures 7c and 7f). As LVW viscosity decreases mantle wedge and slab velocities increase, but the overall pattern of flow is not strongly dependent on wedge viscosity.

### 3.2.1. Flow Focusing With a Free Slab

[28] Sinking of the free slab adjacent to a LVW is characterized by near vertical flow of the slab, with poloidal flow (corner-flow) through the LVW for most of the length of the slab (Figures 5a and 5b). Near the edges a weak toroidal flow brings material from near the slab edges into the sides of the LVW (Figure 5c). The flow magnitudes are fastest in the LVW, in the slab and just below the slab.

[29] The addition of a LVW to free slab models with a slab viscosity of  $10^2$  to  $10^4$  greater than the reference viscosity (Fw1–Fw6) results in the same dependence of slab sinking rate on slab strength, and only a 10% increase in slab sinking rate due to the decrease in viscosity in the LVW adjacent to the slab from  $10^{-1}$  to  $10^{-3}$ . However, the velocity magnitude within the LVW increases by 70% due to the decrease in viscosity by two orders of magnitude, regardless of slab strength (Figure 6a). Therefore, the decrease in viscosity within the mantle wedge

has the effect of focusing the slab-induced flow within this low viscosity region, without changing the overall pattern of flow surrounding the slab (Figures 7a–7c).

[30] The flow focusing ratio increases from  $F = 0.55\text{--}0.6$  for  $\eta'_{min} = 10^{-1}$  to over 0.9 for  $\eta'_{min} = 10^{-3}$  (Figure 6b). Therefore, while the presence of the LVW does not lead to substantial increases in mantle or slab flow rates for free slab models, it does act to localize the slab-induced return flow within the LVW near the slab. Also note that the velocity magnitudes are not as large as those predicted in the recent non-Newtonian models discussed in the introduction. In work by Jadamec and Billen [2010] the non-Newtonian rheology led to a reduction of the viscosity within approximately 500 km surrounding the slab suggesting that a reduction in the background viscous support of the slab is important in generating rapid mantle flow, as demonstrated with the models and analytic solution presented in Section 3.1. Fast

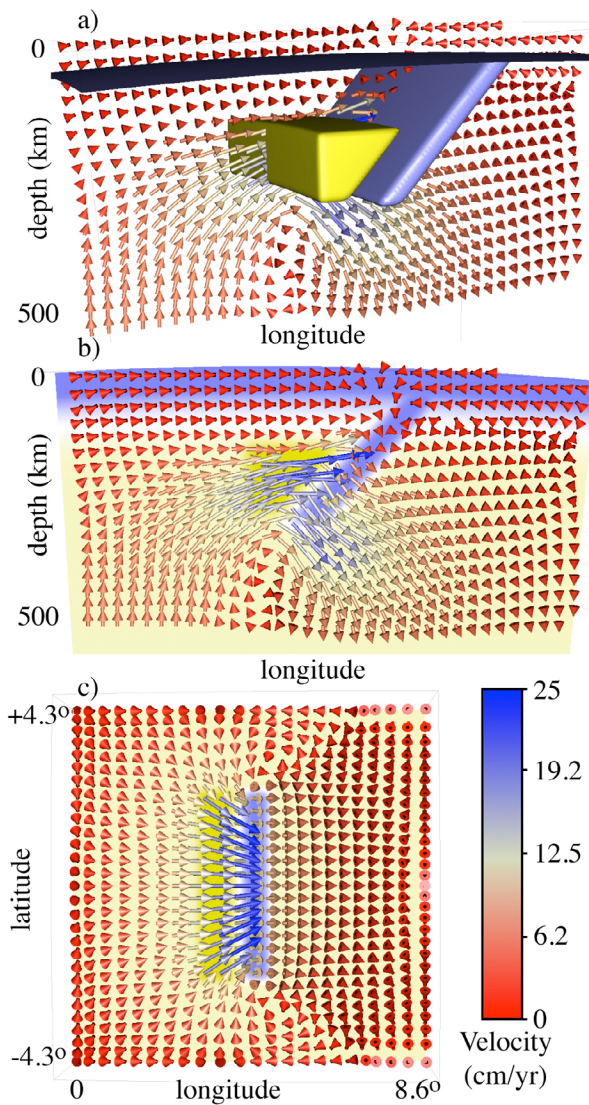


**Figure 8.** 3D flow for attached slab model Aw4R10 ( $\eta_{ref} = 10^{19}$  Pa·s;  $\eta_{wk} = 10^{-2}\eta_{ref}$ ,  $\eta_{slab} = 10^4\eta_{ref}$ ). (a) 3D perspective of cross section of flow ( $0^\circ$  latitude) with viscosity isosurfaces for the imposed weak region and slab. Note retrograde, pivoting motion of deep portion of attached slab. Isosurfaces of weak region and slab in yellow and blue, respectively. Same isosurface and viscosity color scale as in Figure 1. (b) Cross section (same as in Figure 8a) showing asymmetric flow that is cut-off by strong attached-slab. (c) Map view at  $\sim 150$  km depth showing horizontal flow focused within the weak region. Color slice in Figures 8b and 8c is viscosity for reference, using the same color scale as in Figure 1. Only a portion of the domain and flow are shown.

wedge flow velocities (greater than 50–100 cm/yr) are generated in free-slab models with a LVW when the reference viscosity is decreased by 10–100 (Models Fw2R10, Fw2R100, Fw4R10, Fw4R100; Table 3 and Figure 6c).

### 3.2.2. Flow Focusing With an Attached Slab

[31] Sinking of an attached slab adjacent to a LVW (Aw, Table 3) is characterized by a radially-dipping flow oriented perpendicular to the slab surface, with flow magnitude in the slab increasing with depth (Figure 8a). This dipping flow reflects what would be pivoting (steepening) motion of the slab in time-dependent models as the top of the slab is subject to significant resistance to flow, whereas the tip of the slab has very little resistance to sinking. Indeed, in these simple models the slab is essentially fixed to an almost stationary lithosphere because there is no weak plate boundary shear zone (separating the subducting and overriding plates) to direct the sinking motion of the slab to the subducting plate at the surface. The dipping flow within and below the slab drives a poloidal flow (corner-flow) through the LVW with a significant upward component of flow within the wedge corner over most of the length of the slab (Figure 8b). Similar to the free slab models, near the edges of the slab a weak toroidal flow brings material from near the slab edges into the sides of the weak region, but the flow in these models is primarily slab-perpendicular. The flow magnitude is largest in the LVW and just below and behind the free tip of the slab. We note that if a low viscosity shear zone were included in the model this would increase the radial component of flow in the slab.

[32] Flow focusing occurs with attached slab models, even without an imposed LVW, due to the flow geometry generated by a pivoting slab (see section 3.1, Table 2 and Figure 4b). However, addition of a LVW increases the degree of flow focusing and further localizes this flow within the LVW (Models Aw1–Aw6, Table 3). We find the same dependence of slab sinking rate on slab strength (10–20% increase) and a 55–65% increase in mantle wedge velocity due to the decrease in the LVW viscosity from  $10^{-1}$  to  $10^{-3}$ , regardless of slab strength (Figures 7d–7f). We also find no change in the character of the flow when the models are run forward in time (Aw2, A2nn2).

### 3.2.3. Geometric Effects of Strong Slab and Lithosphere

[33] The major difference between free-slab and attached-slab models is in the degree of flow focusing within the mantle wedge for models with a LVW, regardless of the reduction in wedge viscosity. All of the LVW models exhibit faster flow within the mantle wedge than within the slab itself ( $F > 1$ , Table 3 and Figure 7). The flow focusing ratio increases from  $F = 1.09$  to 1.55 for a decrease

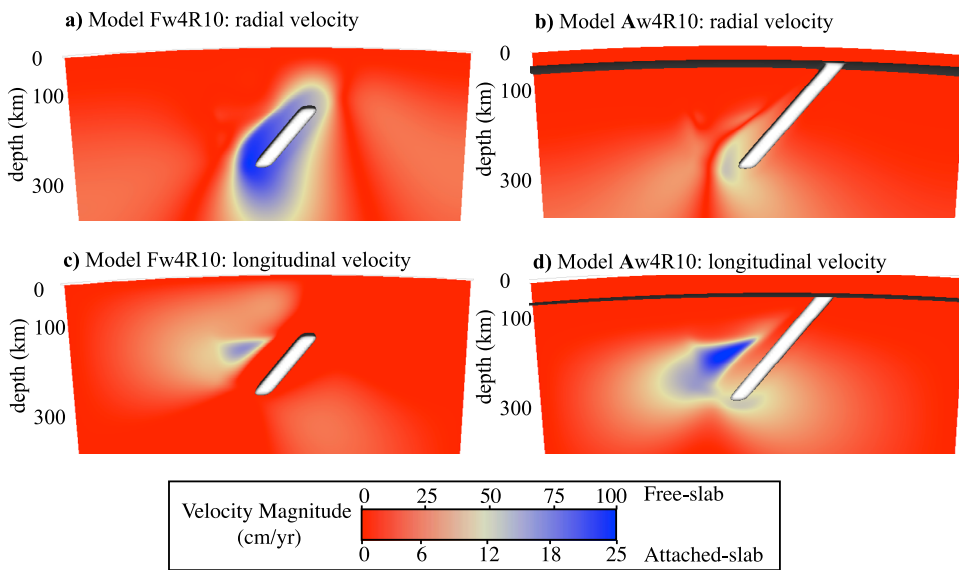


**Figure 9.** Comparison of flow components for (a, c) free slab (model Fw4R10) and (b, d) attached slab (model Aw4R10) models. Radial (Figures 9a and 9b) and longitudinal (Figures 9c and 9d) component of velocity along a cross section at the center of the slab. Radial flow in the slab induces focused lateral flow in the LVW for free-slab models, whereas retrograde pivoting motion (roughly equal radial and longitudinal components) of the tip of the attached slab induces strong lateral flow in the LVW.

in the mantle wedge viscosity from  $10^{-1}$  to  $10^{-3}$  for a slab viscosity of  $10^2$ , while the increase in flow focusing ratio is larger ( $F = 1.59\text{--}2.18$ ) for a slab viscosity of  $10^4$ . However, while the absolute values of  $F$  are larger than those found for the free-slab models,  $F$  increases by about 65% for a decrease in the mantle wedge viscosity from  $10^{-1}$  to  $10^{-3}$  for both the attached-slab models and the free-slab models. Therefore, the faster magnitude flow rates in the mantle wedge region for attached-slab models is not caused by the LVW alone, but instead, is also a result of the change in flow geometry created by a strong slab attached to strong lithosphere and the retrograde, pivoting motion that results.

[34] The flow focusing ratio for the attached slab models without a LVW increases from 0.55, for  $\eta'_{\text{slab}} = 10^0$  to 1.38 for  $\eta'_{\text{slab}} = 10^4$ : a factor of 2.5 increase in the mantle flow rate in the wedge (Table 2). Unlike the free-slab models (with or without a low viscosity wedge), which are characterized by a broad, symmetric poloidal flow cell with roughly equal flow rates converging from either direction above the slab (e.g., Figures 4a and 5) the attached-slab models are characterized by a strongly asymmetric poloidal flow cell that is confined in depth below the lithosphere and is much stronger in magnitude above the slab than it is below or behind the slab (e.g., Figure 4b). This flow

focusing is driven by the pivoting motion of the slab and the fact that there is no return flow above the slab (because it is attached to a stationary plate). Addition of a LVW to the attached slab, therefore, further increases this focusing effect ( $F$  increases from 1.38 to more than 2.0, Figure 9 and Table 3).

[35] This difference in flow behavior and flow focusing for free slabs and attached slabs is further illustrated in Figure 9, which shows the radial and longitudinal flow components for a free slab and an attached slab. The free slab has a strong radial flow driven by sinking of the slab and the reduction in viscosity within the LVW focuses the horizontal (longitudinal) component of flow within the LVW (Model FwR10, Figures 9a and 9c). In contrast, for the attached slab the radial component of flow is much smaller and is limited to the tip of the slab. Nonetheless this generates a larger longitudinal component of flow within the LVW, generated in part by the retrograde (longitudinal) motion of the slab (Model AwR10, Figures 9a and 9c).

### 3.2.4. Yielding With No Plate Boundary Weak Zone

[36] The influence of slab strength on the flow geometry and localization of fast mantle flow rates is further illustrated by adding the effect of yielding to the models with an attached slab (Table 2 and Figure 3c). For the models presented here with no

plate boundary shear zone to separate the attached slab from the overriding plate, and with a short slab that is not viscously supported by a higher viscosity lower mantle, adding yielding causes the slab to become viscously detached from the subducting plate. The yielding causes the slab viscosity to drop to background viscosity values in a region below the lithosphere. This reduction in viscosity opens a pathway for slab-induced flow just below the lithosphere. The result is flow patterns that are the same as the free-slab models (Figure 3a):  $F = 0.6$  for all models with yielding. However, slab and wedge flow rates for both Newtonian viscosity models (compare A2Y3–A2Y10 to F2) and non-Newtonian models (compare A2nnY3–A2nnY10 to F2nn2) are higher for models with yielding because the slab viscosity is also reduced by yielding.

#### 4. Conclusions

[37] The models presented here demonstrate that faster background mantle flow velocities occur in models with both free and attached slabs when the reference viscosity is low or non-linear rheology leads to equally low viscosities surrounding the sinking slab. These velocities are fastest for completely free slabs (or attached slabs that yield through) and slowest for uniformly strong attached slabs. Agreement of the numerical models, with both Newtonian and non-Newtonian rheology, with the analytic solution for a sinking ellipsoid demonstrates that the fast flow regions are not the result of poorly converged solutions, instantaneous solutions or implementation of the non-linear rheology. Instead fast flow rates are expected due to the decrease in viscous resistance to sinking, as indicated by Jadamec and Billen [2010]. Specifically, the non-Newtonian rheology leads to a lower background viscosity surrounding the slab and has the same effect on the slab sinking rate as decreasing the background viscosity in Newtonian models.

[38] Localization of fast velocities in the mantle wedge is a geometric effect and can be caused by either locally lowering the viscosity of mantle wedge, or by introducing a strong slab, or both. Localization of flow is more effective for attached slabs than for free slabs, because the flow is not able to go up and over the strong slab when it is attached to high viscosity lithosphere. Instead, toroidal flow around the edge of the slab, driven by the pivoting retrograde motion of the short slab, couples to the poloidal flow increasing flow magnitudes in the mantle wedge consistent with previous studies [Kincaid and Griffiths, 2003; Schellart,

2004; Funiciello *et al.*, 2006; Stegman *et al.*, 2006; Di Giuseppe *et al.*, 2008]. In models with a LVW and an attached slab, flow rates in the mantle wedge can be more than two times higher than the slab sinking rate because the geometry (i.e., viscosity structure) focuses the return flow within the lowest viscosity region. In addition, the importance of the pivoting motion of the slab (steepening of dip with time) and toroidal flow in generating the flow focusing within the wedge explains why similarly high mantle flow velocities have not been observed in 2D dynamical models or 3D kinematically-driven wedge models with imposed down-dip sinking of the slab [e.g., Kneller and van Keken, 2008].

[39] These results are consistent with mantle flow velocities predicted around the Alaska slab, in which velocities of 20–35 cm/yr within the slab generate lateral flow in the mantle wedge with magnitudes of 50–67 cm/yr [Jadamec and Billen, 2010, 2012]. Note that in the simple models presented here the fast mantle flow velocities are accompanied by a nearly stationary surface plate because we omitted the shear zone between the overriding and subducting plate in order to more clearly demonstrate the importance of the pivoting motion of the slab. However, Jadamec and Billen [2010, 2012] show that coupling of the fast motion of the slab to the surface plate is controlled by the shear zone viscosity and the yield stress of the slab. Only when non-Newtonian rheology, a moderate yield stress (500 MPa) and a weak shear zone ( $10^{20}$  Pa·s) are used together does the model predict both fast mantle flow velocities, and surface plate velocities and seismic anisotropy orientations that agree with observations by Jadamec and Billen [2010, 2012].

[40] As numerical models continue to improve in their ability to represent the complex geometric and rheologic structures of the earth's mantle, it is likely that we will continue to find surprising results, which challenge the simpler flow structures we've become accustomed to in Newtonian models with limited viscosity ranges. In particular, in 3D models, careful analysis of the combination of effects arising from the 3D thermal and stress-dependent viscosity structures, with emergent low viscosity features arising from non-Newtonian rheology, will be required to fully understand the origin of newly observed flow structures. In addition, these simple models suggest that we should expect diverse flow fields around different subduction zones controlled by the unique geometry of each region and that plate motions do not fully

reflect the complexity or magnitude of the flow in the mantle.

## Acknowledgments

[41] This study was motivated by, and the model set-up was planned through, discussions with Michael Gurnis, Laura Alusic, Carsten Burstedde and Georg Stadler. We also thank Scott King and an anonymous reviewer for the valuable comments and suggestions. Three-dimensional images of the model structure and flow were generated with 3DVisualizer developed by KeckCAVES at UC Davis [Billen et al., 2008]. This research was funded by the National Science Foundation grant EAR-0537995 and Career Award 0748818.

## References

- Alusic, L., M. Gurnis, G. Stadler, C. Burstedde, L. C. Wilcox, and O. Ghattas (2010), Slab stress and strain rate as constraints on global mantle flow, *Geophys. Res. Lett.*, **37**, L22308, doi:10.1029/2010GL045312.
- Andrews, E. R., and M. I. Billen (2009), Rheologic controls on the dynamics of slab detachment, *Tectonophysics*, **464**, 60–69, doi:10.1016/j.tecto.2007.09.004.
- Becker, T. W., and H. Kawakatsu (2011), On the role of anisotropic viscosity for plate-scale flow, *Geophys. Res. Lett.*, **38**, L17307, doi:10.1029/2011GL048584.
- Bell, D. R., G. R. Rossman, J. Maldener, D. Endisch, and F. Rauch (2003), Hydroxide in olivine: A quantitative determination of the absolute amount and calibration of the IR spectrum, *J. Geophys. Res.*, **108**(B2), 2105, doi:10.1029/2001JB000679.
- Billen, M. I., and M. Gurnis (2001), A low viscosity wedge in subduction zones, *Earth Planet. Sci. Lett.*, **193**, 227–236.
- Billen, M. I., and G. Hirth (2005), Newtonian versus non-Newtonian upper mantle viscosity: Implications for subduction initiation, *Geophys. Res. Lett.*, **32**, L19304, doi:10.1029/2005GL023457.
- Billen, M. I., and G. Hirth (2007), Rheologic controls on slab dynamics, *Geochem. Geophys. Geosyst.*, **8**, Q08012, doi:10.1029/2007GC001597.
- Billen, M. I., M. Gurnis, and M. Simons (2003), Multiscale dynamic models of the Tonga-Kermadec subduction zone, *Geophys. J. Int.*, **153**, 359–388.
- Billen, M. I., O. Kreylos, B. Hamann, M. A. Jadamec, L. H. Kellogg, O. Staadt, and D. Y. Sumner (2008), A geoscience perspective on immersive 3D gridded data visualization, *Comput. Geosci.*, **49**(9), 1056–1072, doi:10.1016/j.cageo.2007.11.009.
- Burkett, E. R., and M. I. Billen (2009), Dynamics and implications of slab detachment due to ridge-trench collision, *J. Geophys. Res.*, **114**, B12402, doi:10.1029/2009JB006402.
- Buttles, J., and P. Olson (1998), A laboratory model of subduction zone anisotropy, *Earth Planet. Sci. Lett.*, **164**, 245–262.
- Christensen, D. H., and G. A. Abers (2010), Seismic anisotropy under central Alaska from SKS splitting observations, *J. Geophys. Res.*, **115**, B04315, doi:10.1029/2009JB006712.
- Conder, J. A., and D. A. Wiens (2007), Rapid mantle flow beneath the Tonga volcanic arc, *Earth Planet. Sci. Lett.*, **264**, 299–307, doi:10.1016/j.epsl.2007.10.014.
- Di Giuseppe, E., J. van Hunen, F. Funiciello, and C. Faccenna (2008), Slab stiffness control of trench motion: Insights from numerical models, *Geochem. Geophys. Geosyst.*, **9**, Q02014, doi:10.1029/2007GC001776.
- Fischer, K. M., E. M. Parmentier, A. R. Stine, and E. R. Wolf (2000), Modeling anisotropy and plate-driven flow in the Tonga subduction zone back arc, *J. Geophys. Res.*, **105**(B7), 16,181–16,191, doi:10.1029/1999JB900441.
- Forte, A. M., and J. X. Mitrovica (1996), New inferences of mantle viscosity from joint inversion of long-wavelength mantle convection and post-glacial rebound data, *Geophys. Res. Lett.*, **23**(10), 1147–1150, doi:10.1029/96GL00964.
- Funiciello, F., M. Moroni, C. Piromallo, C. Facenna, A. Cenedese, and H. A. Bui (2006), Mapping mantle flow during retreating subduction: Laboratory models analyzed by feature tracking, *J. Geophys. Res.*, **111**, B03402, doi:10.1029/2005JB003792.
- Gerya, T. (2010), *Introduction to Numerical Geodynamic Modelling*, Cambridge Univ. Press, Cambridge, U. K.
- Hirth, G., and D. Kohlstedt (2003), Rheology of the upper mantle and the mantle wedge: A view from the experimentalists, in *Inside the Subduction Factory*, *Geophys. Monogr. Ser.*, vol. 138, edited by J. Eiler, pp. 83–105, AGU, Washington, D. C., doi:10.1029/138GM06.
- Höink, T., and A. Lenardic (2010), Long wavelength convection, poiseuille-couette flow in the low-viscosity asthenosphere and the strength of plate margins, *Geophys. J. Int.*, **180**, 23–33, doi:10.1111/j.1365-246X.2009.04404.x.
- Jadamec, M. A. (2008), 3D numerical models of lithosphere and mantle deformation in southern Alaska, PhD thesis, Univ. of Calif., Davis.
- Jadamec, M. A., and M. I. Billen (2010), Reconciling surface plate motions with rapid three-dimensional mantle flow around a slab edge, *Nature*, **465**, 338–341, doi:10.1038/nature09053.
- Jadamec, M. A., and M. I. Billen (2012), The role of rheology and slab shape on rapid mantle flow: Three-dimensional numerical models of the Alaska slab edge, *J. Geophys. Res.*, doi:10.1029/2011JB008563, in press.
- Kaminiski, É., and N. M. Ribe (2002), Timescales for the evolution of seismic anisotropy in mantle flow, *Geochem. Geophys. Geosyst.*, **3**(8), 1051, doi:10.1029/2001GC000222.
- Karato, S., and P. Wu (1993), Rheology of the upper mantle: A synthesis, *Science*, **260**, 771–778.
- Karato, S., H. Jung, I. Katayama, and P. Skemer (2008), Geodynamic significance of seismic anisotropy of the upper mantle: New insights from laboratory studies, *Annu. Rev. Earth Planet. Sci.*, **36**, 59–95, doi:10.1146/annurev.earth.36.031207.124120.
- Kerr, R. C., and J. R. Lister (1991), The effects of shape on crystal settling and on the rheology of magmas, *J. Geol.*, **99**(3), 457–467.
- Kincaid, C., and R. W. Griffiths (2003), Laboratory models of the thermal evolution of the mantle during rollback subduction, *Nature*, **425**, 58–62.
- Kneller, E. A., and P. E. van Keken (2007), Trench-parallel flow and seismic anisotropy in the Mariana and Andean subduction systems, *Nature*, **450**, 1222–1225, doi:10.1038/nature06429.
- Kneller, E. A., and P. E. van Keken (2008), Effect of three-dimensional slab geometry on deformation in the mantle wedge: Implications for shear wave anisotropy, *Geochem. Geophys. Geosyst.*, **9**, Q01003, doi:10.1029/2007GC001677.

- Long, M., and P. G. Silver (2008), The subduction zone flow field from seismic anisotropy: A global view, *Science*, **319**, 315–318, doi:10.1126/science.1150809.
- Moresi, L., and M. Gurnis (1996), Constraints on the lateral strength of slabs from three-dimensional dynamic flow models, *Earth Planet. Sci. Lett.*, **138**, 15–28.
- Moresi, L., S. Zhong, and M. Gurnis (1996), The accuracy of finite element solutions of Stokes' flow with strongly varying viscosity, *Earth Planet. Sci. Lett.*, **97**, 83–94.
- Russo, R. M., and P. G. Silver (1994), Trench-parallel flow beneath the Nazca Plate from seismic anisotropy, *Science*, **263**(5150), 1105–1111.
- Schellart, W. P. (2004), Kinematics of subduction and subduction-induced flow in the upper mantle, *J. Geophys. Res.*, **109**, B07401, doi:10.1029/2004JB002970.
- Schubert, G., D. L. Turcotte, and P. Olson (2001), *Mantle Convection in the Earth and Planets*, Cambridge Univ. Press, New York.
- Smith, G. P., D. A. Wiens, K. M. Fischer, L. M. Dorman, S. C. Webb, and J. A. Hildebrand (2001), A complex pattern of mantle flow in the Lau backarc, *Science*, **292**, 713–716.
- Stadler, G., M. Gurnis, C. Burstedde, L. C. Wilcox, L. Alisic, and O. Ghattas (2010), The dynamics of plate tectonics and mantle flow: From local to global scales, *Science*, **329**, 1033–1037, doi:10.1126/science.1191223.
- Stegman, D. R., J. Freeman, W. P. Schellart, L. Moresi, and D. May (2006), Influence of trench width on subduction hinge retreat rates in 3-D models of slab rollback, *Geochem. Geophys. Geosyst.*, **7**, Q03012, doi:10.1029/2005GC001056.
- Tan, E., E. Choi, P. Thoutireddy, M. Gurnis, and M. Aivazis (2006), GeoFramework: Coupling multiple models of mantle convection within a computational framework, *Geochem. Geophys. Geosyst.*, **7**, Q06001, doi:10.1029/2005GC001155.
- Turcotte, D. L., and G. Schubert (1982), *Geodynamics*, 1st ed., John Wiley, New York.
- Zhong, S. (2006), Constraints on thermochemical convection of the mantle from plume heat flux, plume excess temperature, and upper mantle temperature, *J. Geophys. Res.*, **111**, B04409, doi:10.1029/2005JB003972.
- Zhong, S., M. T. Zuber, L. Moresi, and M. Gurnis (2000), Role of temperature-dependent viscosity and surface plates in spherical shell models of mantle convection, *J. Geophys. Res.*, **105**, 11,063–11,082.